[Short title + Author Name - P&H title] 17 (2024) 105907

Contents lists available at ScienceDirect

Arabian Journal of Chemistry

journal homepage: www.ksu.edu.sa

Highly efficient crystalline-amorphous Fe_2O_3/Fe-OOH oxygen evolution electrocatalysts reconstructed by FeS_2 nanoparticles

Xiaozhen Ren *, Shanshan Li, Ziyou Li, Zhenyang Zhang, Hanxu Hou, Yanan Zhou, Chuanyu Jin *

School of Materials Science and Engineering, Liaocheng University, Liaocheng 252000, China

ARTICLE INFO

Keywords:
Bimetallic sulfide
Self reconstruction
Crystalline-amorphous
Fe_2O_3/Fe-OOH
OER

ABSTRACT

It is crucial to explore the earth-abundant, high-efficient and stable electrocatalysts suitable for accelerating water splitting kinetics of oxygen evolution reaction (OER) in alkaline electrolytes. Herein, $Fe_xCo_{1-x}S_2$ (x = 0, 0.25, 0.5, 0.75 and 1) nanoparticles were fabricated via hydrothermal method and sulfidizing. Remarkably, the FeS_2 delivers the most outstanding OER activity among prepared catalysts, with the overpotential of 240 mV for 10 mA/cm^2, ultra-low Tafel slope of 45 mV/decades and high stability for 16 h. XRD, SEM, HRTEM, Raman and XPS characteristics before and OER process, TOF and electrochemical results indicate that surface reconstruction, strong combination of Fe-S and uniform dispersion of particles endow FeS_2 with excellent catalytic property. The strong combination of Fe-S bond and uniform dispersion of FeS_2 facilitates electron transfer. And the reconstructed crystalline-amorphous Fe_2O_3/FeOOH with rough surface may have a low energy barrier for the elementary reaction of O*→OOH*, which is responsible for boosting the generation of O_2. In the practical two-electrode overall water splitting system in 1 M KOH, the FeS_2/NF//Pt/C/NF system only needs an ultra-low cell voltage of 1.46 and 1.642 V to generate the current densities of 10 and 50 mA/cm^2, respectively.

1. Introduction

Hydrogen is widely regarded as a key component in future energy systems just as it is a clean, sustainable and transportable energy carrier (Pomerantseva et al., 2019; Jiao et al., 2015; Zhang et al., 2023a; Zhang et al., 2023b). Electrocatalytic water splitting, which can driven by electricity of power grid, solar energy and rechargeable batteries (Rebrov and Gao, 2023; Kang et al., 2021) is extensively considered an environmentally friendly and efficient hydrogen production technology (Suen et al., 2017; Gong et al., 2013; He et al., 2024). Compared with the hydrogen evolution reaction (HER), the electrocatalytic efficiency is severely restricted by the oxygen evolution reaction (OER) process because of the slow kinetics and high overpotentials resulting from the complex four-electron transfer (Zhang et al., 2023a; Zhang et al., 2023b; Wang et al., 2020d; Wang et al., 2023d). So, there is a pressing need to explore highly efficient, low-cost and earth-abundant electrocatalysts with fast kinetics and low overpotential for water splitting. Despite noble metal catalysts have proven to be desirable catalysts for OER, the high cost and scarcity of resources seriously limited their wide applications (Ying et al., 2018; Su et al., 2024).

So far, various non-precious materials, including metal oxides (Zhang et al., 2020), phosphate (Li et al., 2022), chalcogenides (Yue et al., 2023), and hydroxides (Peng et al., 2023) have been designed to catalyze the OER, in which Cobalt (Co) or iron (Fe)-based chalcogenides, such as CoFe-Co_8FeS_8(Wang et al., 2019), Co_8FeS_8/CoS (Wang et al., 2020a), are excellent candidates towards OER because of their good electronic conductivity and their rich redox properties. Among them, MS_2 (M=Fe, Co) deliver high electrocatalytic activity towards OER (Li et al., 2018; Wang et al., 2023c; Xie et al., 2022). Li et al prepared Fe_7S_8/FeS_2/C (Xu et al., 2021) electrocatalysts, in which only 262 mV of overpotentials was required to reach 10 mA/cm^2 towards OER. The synthesized $FeCoS_2$/Co_4S_3/NFG catalysts exhibited enhanced OER catalytic activity, with an overpotential of 276 mV for OER at 10 mA/cm^2 (Wang et al., 2023c). Until now, we should also do much research on preparing MS_2 (M=Fe, Co) catalysts with improved electrocatalytic performance and reduced energy consumption.

Exploring the real active site during the OER process in alkaline environments is very important for improving the catalytic performance. Recently, a large number of researchers has put forward a view that the prepared electrocatalysts are not real “catalysts”, but “pre-

* Corresponding authors at: 1 Hunan Road, Liaocheng City, Shandong Province, China.
E-mail addresses: renxiaozhen@lcu.edu.cn (X. Ren), jinchuanyu@lcu.edu.cn (C. Jin).

https://doi.org/10.1016/j.arabjc.2024.105907
Received 26 March 2024; Accepted 10 July 2024
Available online 11 July 2024

catalysts", for which their morphology, composition and phase changed dramatically (Chen et al., 2018; Wang et al., 2018; Ren et al., 2023). Huang et al (Su et al., 2024) found that the prepared RuO_2/Co_3O_4 had reconstructed to RuO_2/CoOOH during the OER process, which showed a low energy barrier for the reaction of O* to *OOH to improve OER performance. Liu et al (Yue et al., 2023) proved that FeS_2@FeOOH reconstructed by FeS_2 microspheres during the OER process was responsible for the improved OER activity. Also, the high entropy sulfide of $FeNiCoCrMnS_2$ was reconstructed to the metal (oxy)hydroxide during the OER process (Nguyen et al., 2021). Whereas, studying the synergistic effect of Co contents and reconstructing influence on Fe/S catalysts is still rare.

In this study, $Fe_xCo_{1-x}S_2$ (x = 0, 0.25, 0.5, 0.75 and 1) nanoparticles supported on Ni foam were designed, which exhibit excellent OER activity in alkaline environments. The electrochemeical measurements of LSV, CV, EIS, i-t for $Fe_xCo_{1-x}S_2$ catalysts were performed to evaluate the electrocatalytic activity for OER. Remarkably, the FeS_2 delivers the most outstanding OER activity among prepared $Fe_xCo_{1-x}S_2$ catalysts. The strong combination of Fe-S bond and uniform dispersion endow FeS_2 fast electron transfer. By comparing with XRD, XPS, SEM, TEM and HRTEM, we found that the crystalline-amorphous Fe_2O_3/Fe-OOH with the rough surface after OER reconstructed by FeS_2 supported on Ni foam is the real active site. The reconstructed crystalline-amorphous Fe_2O_3/Fe-OOH may have a low energy barrier for the elementary reaction of O*→OOH*. Moreover, it only requires the voltage of 1.460 and 1.642 V to generate the current density of 50 and 100 mV/cm^2 in a practical two-electrode overall water splitting system. This study may provide a new idea for the research of metal sulfide electrocatalysts toward OER for alkaline water splitting systems.

2. Experimental section

2.1. Samples preparation

As shown in Scheme 1, for preparing CoS_2 nanoparticles: 0.6 g Lysine was added to 75 mL $CoCl_2$ solution (0.05 mol/L) and stirred at 40 °C for 0.5 h in a water bath. 4 mL of ammonia water (32 wt%) was evenly added to the solution within 0.5 h using a peristaltic pump. After stirring the solution for 0.5 h, transfer it into a 100 mL Teflflon-lined autoclave and heat it in an oven at 180 °C for 6 h. After centrifugal, washing and drying for three times, the obtained powder was vacuum-dried overnight at 60 °C. The dried sample was thoroughly mixed with sublimed sulfur at a mass ratio of 1:5, and ground for 10 min. The final CoS_2 sample was obtained by calcining the mixed powder at 450 °C in N_2 atmosphere for 4 h, with a heating rate of 5 °C/min.

For preparing $Fe_xCo_{1-x}S_2$ nanoparticles: the synthesis process is similar to the above except for changing the amounts of the added salts. For x = 0, 0.25, 0.5, 0.75 and 1, the amounts of added $CoCl_2$ are 75 mL, 56.25 mL, 37.5 mL, 18.75 mL, and 0 mL while the amounts of added $FeCl_3$ are 0 mL, 18.75 mL, 37.5 mL, 56.25 mL, and 75 mL, and the samples are marked with CoS_2, $Fe_{0.25}Co_{0.75}S_2$, $Fe_{0.5}Co_{0.5}S_2$, $Fe_{0.75}Co_{0.25}S_2$, and FeS_2, respectively.

2.2. Material characterizations

The surface structure, morphology and interior structure of the synthetic samples were analyzed by emission scanning electron microscope (FESEM, Zeiss Sigma, Japan) equipped with energy-dispersive X-ray spectroscopy (EDS) and high-resolution transmission electron microscope (HRTEM, FEI Tecnai F30, America). The crystal structures of the samples were investigated using X-ray diffraction (XRD, Smartlab, Rigaku, Japan) with a CuKα radiation source. The elementary composites and surface chemical status of the samples were inspected by performing X-ray photoelectron spectroscopy (XPS, ESCALAB 250xi) and Raman spectroscopy (Raman, Thrmo DXRxi).

2.3. Electrochemical measurements

All the electrochemical measurements were performed by using an electrochemical workstation of Gamry, equipped with a conventional three-electrode cell. In the three-electrode system, Ni foam (1 × 1 cm^2) coated with our samples, graphite rod, and Hg/HgO served as working electrode, counter electrode, and reference electrode, respectively. The working electrode was prepared as follow: 10 mg catalysts and 1.0 mg conductive carbon were dispersed onto a mixture of 400 μL isopropanol and 80 μL Nafion solution (5 %, DuPont) with ultrasound for 90 min. After that the prepared homogeneous ink was uniformly dropped onto the pre-treated foam Ni. The conducted potentials in this measuring system were converted to the reversible hydrogen electrode (RHE) potential using the following equation:

$$E_{RHE}=E_{Hg/HgO}+0.059\ pH+0.098$$

LSV cures were conducted at a scan rate of 5 mV/s in the range of 0–1 V *vs.* Hg/HgO with 95 % iR-corrected. Cyclic voltammetry (CV) scanning was carried out in 1 M KOH and was used to inspect the electrochemical double-layer capacitance (C_{dl}) and the roughness factor (R_f) of the samples according to the equation: $R_f = C_{dl}/60$, where 60 represents the assumed 60 uF/cm^2 for the double layer capacitance of a smooth surface (Zhang et al., 2013).

Electrochemical impedance spectroscopy (EIS) was conducted to collect the Nyquist plots towards OER. To evaluate the OER stability, a

Scheme 1. The preparing procedure of the $Fe_xCo_{1-x}S_2$ nanoparticles.

chronopotentiometry test was performed for 16 h at a potential of 1.547 *vs.* RHE.

Also, a two-electrode system was set up for practical overall water splitting. All the two- and three-electrode systems are alkaline solutions with 1.0 M KOH.

3. Results and discussion

3.1. Characterization and electrocatalytic performance for OER

The surface structure and morphologies of CoS_2, $Fe_{0.25}Co_{0.75}S_2$, $Fe_{0.5}Co_{0.5}S_2$, $Fe_{0.75}Co_{0.25}S_2$ and FeS_2 were investigated by the FESEM, as shown in Fig. 1. All the $Fe_xCo_{1-x}S_2$ (x = 0, 0.25, 0.5, 0.75, 1) samples are composed of nanoparticles. In Fig. 1a, the CoS_2 is made up of very fine nanoparticles. Interestingly, by increasing the x value from 0 to 1 for $Fe_xCo_{1-x}S_2$, the sample became more bigger and uniform, with more smoother surfaces. The uniform particle dispersion is beneficial to electron transport, thereby improving electrochemical performance and reducing resistance for OER (Wang et al., 2022). The elemental mapping of FeS_2 in Fig. 1f indicates that the dispersion of S and Fe elements is consistent.

TEM and HRTEM were carried out to inspect the interior structure of the synthetic FeS_2 sample, as displayed in Fig. 2. Fig. 2a-2b show that the FeS_2 nanoparticles are uniformly dispersed with the size of 50 nm, which is consistent with the results in Fig. 1e-1f. The HRTEM images in Fig. 2c-2f clearly show that the particles have a clear and smooth surface, which will under significant changes during the OER process. Additionally, the determined lattice fringes are 0.27, 0.31, and 0.19 nm, corresponding to the (200), (111), and (220) planes of FeS_2 (PDF#71–1680), respectively.

XRD patterns of various samples are shown in Fig. 3. In the patterns of CoS_2, the diffraction peaks at 27.878°, 32.300°, 36.237°, 39.835°, 46.329° and 54.938° are attributed to (111), (200), (210), (211), (220), and (311) planes of CoS_2 (PDF#89–1492). With increasing the amounts of Fe, all the diffraction peaks shifted towards the large 2θ for the $Fe_{0.5}Co_{0.5}S_2$, $Fe_{0.75}Co_{0.25}S_2$ and FeS_2. This phenomenon is attributed to that the radius of Fe is smaller than that of Co. In the patterns FeS_2, the (111), (200), (210), (211), (220), and (311) planes match well with the 2θ of 28.516°, 33.045°, 37.079°, 40.768°, 47.431°, 56.278° and belong to FeS_2 (PDF#71–1680). The XRD patterns of the samples indicate that we have obtained the pure CoS_2, $Fe_{0.5}Co_{0.5}S_2$, $Fe_{0.75}Co_{0.25}S_2$, and FeS_2.

XPS was performed to inspect the elementary composites and surface chemical status of the samples. The XPS full spectra in Fig. S1a show the obvious Co 2p, Fe 2p and S 2p peaks. The binding energies at 708.0 and 720.8 eV in Fig. S1b are assigned to $Fe_{(II)}$-S $2p_{3/2}$ and $Fe_{(II)}$-S $2p_{1/2}$, respectively, while the peaks at 711.2 and 724 eV consist to $Fe_{(III)}$-S $2p_{3/2}$ and $Fe_{(III)}$-S $2p_{1/2}$ (Guo et al., 2020). Similarly, the XPS spectrum of Co 2p in Fig. S1c all can be decomposed into four peaks, where the binding energies at 778.9 and 798.7 eV belong to $Co_{(II)}$-S $2p_{3/2}$ and $Co_{(II)}$-S $2p_{1/2}$. The other peaks at 782.9 and 803.8 eV are attributed to $Co_{(III)}$-S $2p_{3/2}$ and $Co_{(III)}$-S $2p_{1/2}$, respectively (Fang et al., 2017; Yan et al., 2020). The two peaks at 163.2 and 164.5 eV for the S spectrum in Fig. S1d are assigned to S $2p_{3/2}$ and S $2p_{1/2}$ from metal sulfide. In addition, the peak at 169.3 eV may be due to the high oxidized sulfur species on the surface of $Fe_{0.25}Co_{0.75}S_2$ samples (Khani and Wipf, 2017). The Raman spectra for CoS_2, $Co_{0.25}Fe_{0.75}S_2$ and FeS_2 in Fig. S2 show that the peaks at around 386 to 368 cm^{-1} correspond to Co (Fe)-S bond. Interestingly, the peaks shifted towards lower cm^{-1}, which means the the binding energy became stronger by x increasing for $Fe_xCo_{1-x}S_2$, further effecting their ability for electrons transfer.

The LSV polarization curve was conducted to probe the OER performance of the various electrocatalysts, as displayed in Fig. 4a, and the corresponding overpotentials at 10, 50, and 100 mA/cm^2 were shown in Fig. 4b. The overpotentials of CoS_2, $Fe_{0.25}Co_{0.75}S_2$, $Fe_{0.5}Co_{0.5}S_2$, $Fe_{0.75}Co_{0.25}S_2$, and FeS_2 at 10, 50, and 100 mA/cm^2 are all smaller than that of Ni foam and benchmarking RuO_2, indicating the prepared $Fe_xCo_{1-x}S_2$ (x = 0, 0.25, 0.5, 0.75, 1) samples could act as an excellent catalyst for OER reaction under alkaline condition. Remarkably, the FeS_2 delivers the most outstanding OER activity, and it just needs a low overpotentials of 240, 280, and 300 mV to gain the current densities of 10, 50, and 100 mA/cm^2, respectively. It is worth noting that the improved OER performance from CoS_2 to FeS_2 by increasing the x in $Fe_xCo_{1-x}S_2$ may be attributed to the uniform dispersion, the clear and smooth surface and the inherent properties of Fe and Co bimetals, which will be beneficial to electron transport, consistent with the result in Figs. 1-2. On the other hand, the turnover frequency (TOF), acting as the intrinsic activity for the electrocatalysts during the OER process, was calculated with the overpotential of 300 mV and was shown in Supporting Information. The order of the oxygen binding sites for FeS_2,

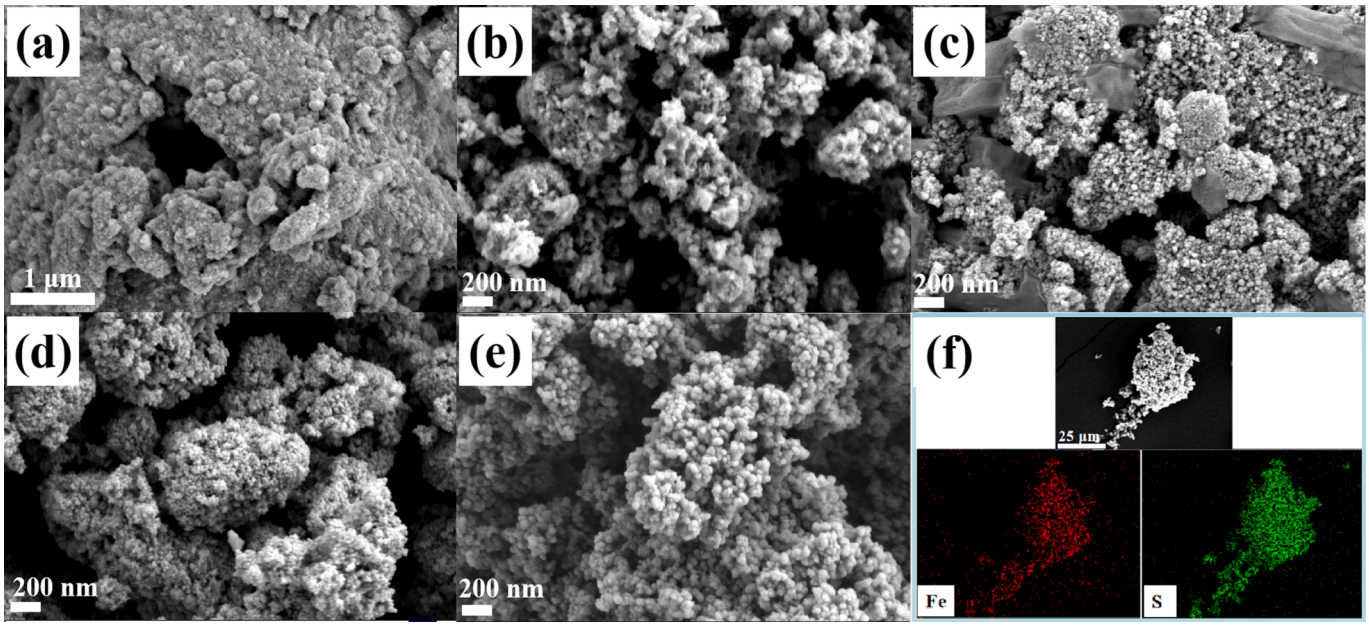

Fig. 1. SEM images of (a) CoS_2 (b) $Fe_{0.25}Co_{0.75}S_2$ (c) $Fe_{0.5}Co_{0.5}S_2$ (d) $Fe_{0.75}Co_{0.25}S_2$ (e) FeS_2 and (f) elemental mapping of FeS_2.

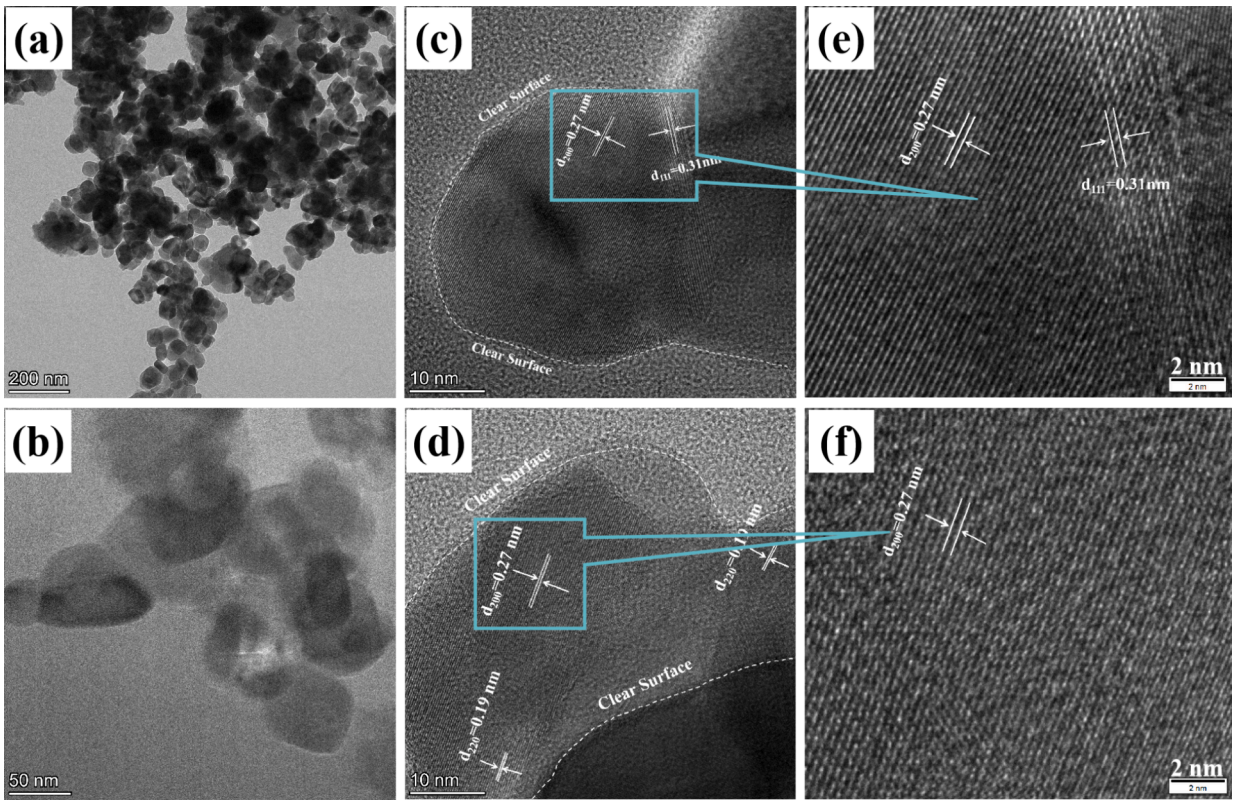

Fig. 2. TEM and HRTEM of FeS_2 before OER.

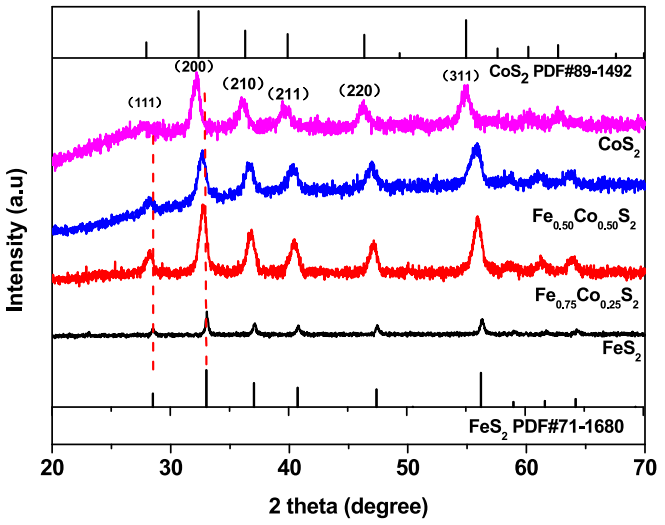

Fig. 3. XRD patterns of prepared samples.

$Fe_{0.75}Co_{0.25}S_2$, $Fe_{0.5}Co_{0.5}S_2$, $Fe_{0.25}Co_{0.75}S_2$ and CoS_2 are 5.01983 > 4.98769 > 4.95594 > 4.92488 > 4.89366, indicating that FeS_2 has the most strongest binding ability among the $Fe_xCo_{1-x}S_2$ samples. So, the TOFs of FeS_2, $Fe_{0.75}Co_{0.25}S_2$, $Fe_{0.5}Co_{0.5}S_2$, $Fe_{0.25}Co_{0.75}S_2$, CoS_2, and RuO_2 are 0.03108, 0.01254, 0.00701, 0.00668, 0.00155, and 0.00154 O_2 per s per site, respectively. Astonishingly, the TOF of FeS_2 is 20 times more than that of CoS_2, confirming the highest intrinsic activity for FeS_2.

Tafel plots, reflecting the reaction kinetic of OER, were calculated from LSV data, as shown in Fig. 4c. The Tafel slopes of $Fe_xCo_{1-x}S_2$ catalysts are smaller than that of Ni foam and RuO_2, indicating that they are easier for overcoming the reaction kinetic process than commercial RuO_2. The smallest Tafel slope of 45 mV/decade for FeS_2 means it needs overcome the smallest energy barrier during the $Fe_xCo_{1-x}S_2$ samples. Table 1 indicates that the overpotentials at 10 mA/cm^2 and the Tafel slopes of prepared $Fe_{0.75}Co_{0.25}S_2$ and FeS_2 catalysts are equal to or even lower than that of the most of the reported transition metal/S-based OER electrodes, further implying the competitiveness of prepared electrocatalysts. Similarly, the FeS_2 had the smallest R_{ct} value, further demonstrating the most accelerated charge transport kinetics during the OER process, Fig. 4d. Furthermore, the contact angle measurement was conducted to evaluate the penetration of the electrolyte into the FeS_2 electrode. The FeS_2 electrode exhibits a superhydrophilic behavior, with a contact angle approaching 0° (Fig. S5).

For practical application, it is crucial to estimate the stability of the electrocatalysts during the OER process. We carried out the chronopotentiometry at 1.547 V *vs.* RHE to identify the stability of the FeS_2 catalyst, Fig. 4e. Notably, the current density remained almost unchanged with an approach of 50 mA/cm^2 for 16 h. In addition, As shown in Fig. 4e, the electrocatalytic activity for FeS_2 after 1000 CV cycles changed little compared with that of initial LSV.

The C_{dl} and R_f, which can be determined by cyclic voltammetry (CV) measurements in the non-Faradic regions, are typically indexed to estimate electrochemical surface area (ECSA). According to the CV measurement for Ni foam, $Fe_xCo_{1-x}S_2$ in Fig. S3 at scan rates of 20, 40, 60, 80, 100 mv/s in 1 M KOH, the C_{dl} for FeS_2 is 1.93 mF/cm^2, which is much higher than those of 1.64, 1.62, 0.69, 0.38 and 0.24 mF/cm^2 for $Fe_{0.75}Co_{0.25}S_2$, $Fe_{0.5}Co_{0.5}S_2$, $Fe_{0.25}Co_{0.75}S_2$, CoS_2 and Ni foam, respectively, indicating that FeS_2 possesses the highest ECSA among those various samples and number of active sites, further accelerating the OER process. Moreover, R_f reflects the non-uniformity of the working electrode and a larger R_f means more active surface area for driving the OER process. According to $R_f = C_{dl}/60$, the values of R_f for FeS_2 is 32.1, higher than that of $Fe_{0.75}Co_{0.25}S_2$ (27.3), $Fe_{0.5}Co_{0.5}S_2$ (27), $Fe_{0.25}Co_{0.75}S_2$ (11.5), CoS_2 (6.3) and Ni foam (4) in terms of double-layer capacitance, respectively, implying the most active area for FeS_2.

Considering the practical application of two-electrode electrolysis,

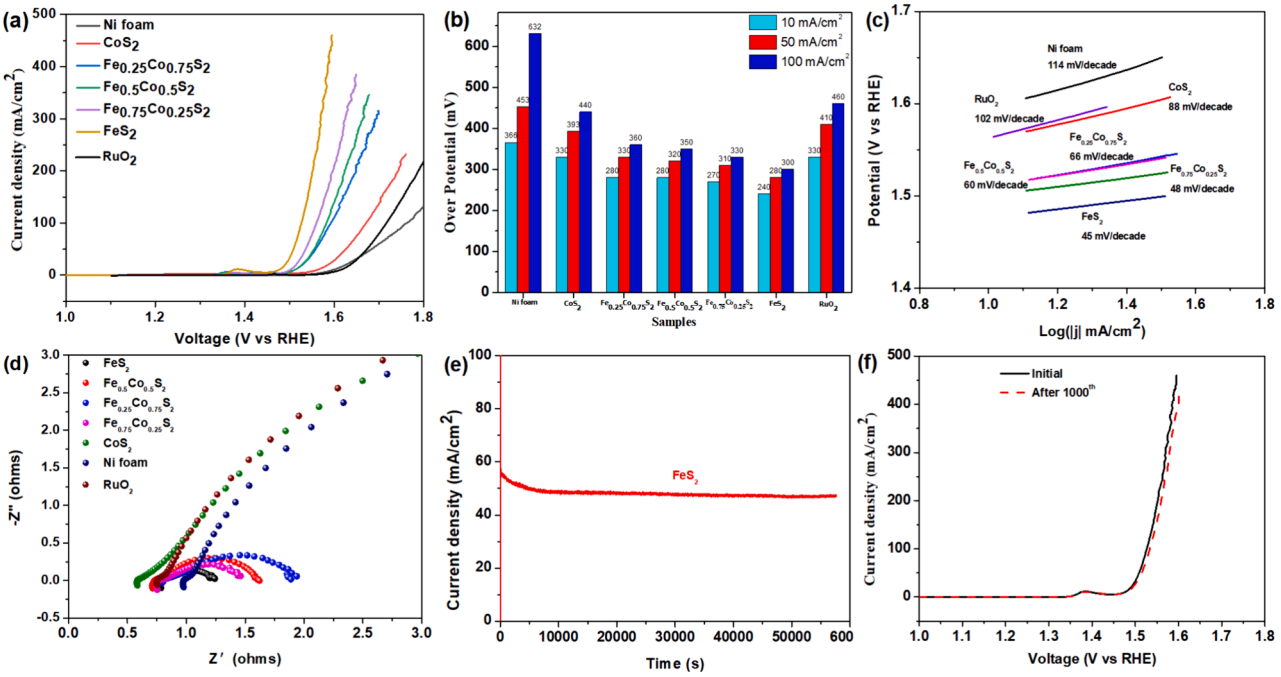

Fig. 4. Electrochemical performances of prepared samples for OER: (a) polarization curve (b) overpotentials at 10, 50, and 100 mA/cm^2 (c) Tafel slopes (d) Nyquist plots in the frequency range of 10^5-0.1 Hz tested in 1 M KOH (e) chronopotentiometry of the FeS_2 catalyst performed under a constant potential of 1.547 V *vs.* RHE for 16 h and (f) polarization curve for FeS_2/NF initial and after 1000 cycles after chronopotentiometry for 16 h.

Table 1
The OER activity of the prepared $Fe_xCo_{1-x}S_2$ (x = 0, 0.25, 0.5, 0.75 and 1) in this work, compared with reported transition metal/S-based OER electrodes in alkaline media (1 M KOH) reported in previous references.

Catalysts	η/mV 10 mA cm^{-2}	Tafel slope /mV dec^{-1}	References
FeS_2	189.5	71	Wang et al., 2021
CoFe-Co_8FeS_8	290	38	Wang et al., 2019
Co_8FeS_8/CoS	278	49	Wang et al., 2020a
Fe_7S_8/FeS_2/C	262	48	Xu et al., 2021
$FeCoS_2$/Co_4S_8/NFG	276	148	Wang et al., 2023c
Ni-Ni_3S_2@carbon NP	284.7	56	Lin et al., 2019
$Co_{0.3}Ni_{0.3}Fe_{0.2}S$ NPs/C	266	47	Wang et al., 2023a
Ni_3S_2/MoS_2	260	59	Wang et al., 2020b
$CoNi_2S_4$@CoS_2	259	45	Huang et al., 2019
Co_9S_8 Hollow Spheres	285	58	Feng et al., 2017
CoS_2 HNSs	290	57	Ma et al., 2018
CoMoOS NBs	281	75.4	Xu et al., 2020
$Fe_{1-x}S$/C	130	55	Wang et al., 2023b
CoS_2-FeS_2	210	46	Wang et al., 2020c
$Fe_{0.75}Co_{0.25}S_2$	270	48	This work
FeS_2	240	45	This work

the overall water splitting for FeS_2/NF and Pt/C/NF (FeS_2/NF//Pt/C/NF) served as an anode and a cathode was performed in 1 M KOH. Meanwhile, we assembled the RuO_2/NF//Pt/C/NF and Ni foam//Ni foam two-electrode systems, displayed in Fig. 5b. Apparently, the FeS_2/NF//Pt/C/NF system just required only 1.460 and 1.642 V to generate the current densities of 10 and 50 mA/cm^2, respectively, which was much lower than those of RuO_2/NF//Pt/C/NF (1.55 and 1.863 V) and Ni foam//Ni foam (1.86 V at 10 mA/cm^2) systems, Fig. 5c. Interestingly, the FeS_2/NF//Pt/C/NF system remained high stability at 123 mA/cm^2 for 16 h, Fig. 5d. All the above results indicates that FeS_2/NF//Pt/C/NF two-electrode system possess high catalytic performance and stability toward the practical overall water splitting.

3.2. Characterization after OER

It is very crucial to get insight into the crystal phase, structure and morphology changes after OER for surveying the catalytic capability, stability and active site for OER catalysts. So, the SEM, TEM, HRTEM, XRD, Raman and XPS were performed to characterize the FeS_2 catalysts after OER. As shown in Fig. 6a and 6b, the FeS_2 samples after OER still kept the morphology of nanoparticles, further implying its stability. Interestingly, the nanoparticles after OER became much smaller, with a more uneven surface. The TEM and HRTEM in Fig. 6d-6 g demonstrated the roughened surface caused by the OER process is very different from the smooth surface in Fig. 2. We also further inspect the diffraction of the catalysts after OER. After magnified in Fig. 6e and 6 g, the single FeS_2 catalyst before OER had largely evolved into crystalline Fe_2O_3 after OER, which could be verified by the (220) planes of FeS_2 and (110) planed of Fe_2O_3, matched with the lattice fringes of 0.19 and 0.25 nm, respectively, accompanying with some amorphous phase of FeOOH marked with a yellow circle. In addition, the mapping in Fig. 6c also showed the dispersed Fe, S and O elements.

In the Raman spectrum of FeS_2 after OER process in Fig. 7a, the peak at 555 cm^{-1} corresponds to the vibration of FeOOH, implying the formation of amorphous CoOOH, while another broad peak around 1050 cm-1 is the signal peak for *OOH (Moysiadou et al., 2020; Koza et al., 2013). The main peaks of Fe, S and O had changed obviously, as shown in Fig. S4. Comparing with Fe 2p before and after OER, it is obvious that the peaks at 708.0 and 720.8 eV belonging to Fe(II) had almost vanished in Fig. 7b (Guo et al., 2020). Meanwhile, the peaks at 711.2 and 724 eV in Fig. 7c belonging to Fe(III) also shifted to 711.6 and 724.4 eV, which could attribute to Fe-O and Fe-OOH bonds (Chen et al., 2022), further proofing the formation of Fe_2O_3 and the amorphous phase of Fe-OOH. It happened that the peak intensities at 162.2 and 163.3 eV belonging to S 2p3/2 and 2p1/2 also became weaker and even disappeared for FeS_2 after OER, while the peak strength at 168.4 eV attributed to SO_4^{2-} became stronger after OER (Wang et al., 2017), resulting from the oxidation for FeS_2, as displayed in Fig. 7c. The O 2p spectrum after OER can be decomposed into Fe-O or Fe-OOH at 531.7 eV and adsorbed H_2O at 533.5 eV, respectively (Abu-Zied and Ali, 2018; Yu et al., 2017), in

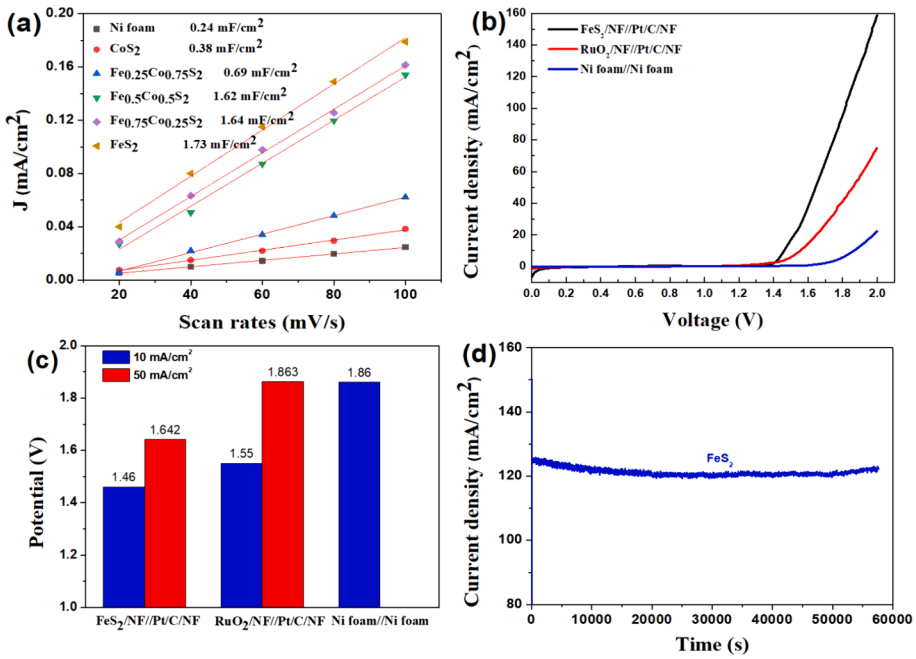

Fig. 5. (a) the plots of the current density *v.s.* scan rates of various samples, (b) the LSV cures, (c) overpotentials at 10 and 50 mA/cm^2 for two electrode water splitting of bare Ni foam//Ni foam, RuO_2/NF//Pt/C/NF, and FeS_2NF//Pt/C/NF systems in 1 M KOH. (d) i-t cures of FeS_2 for water splitting at 1.551 V.

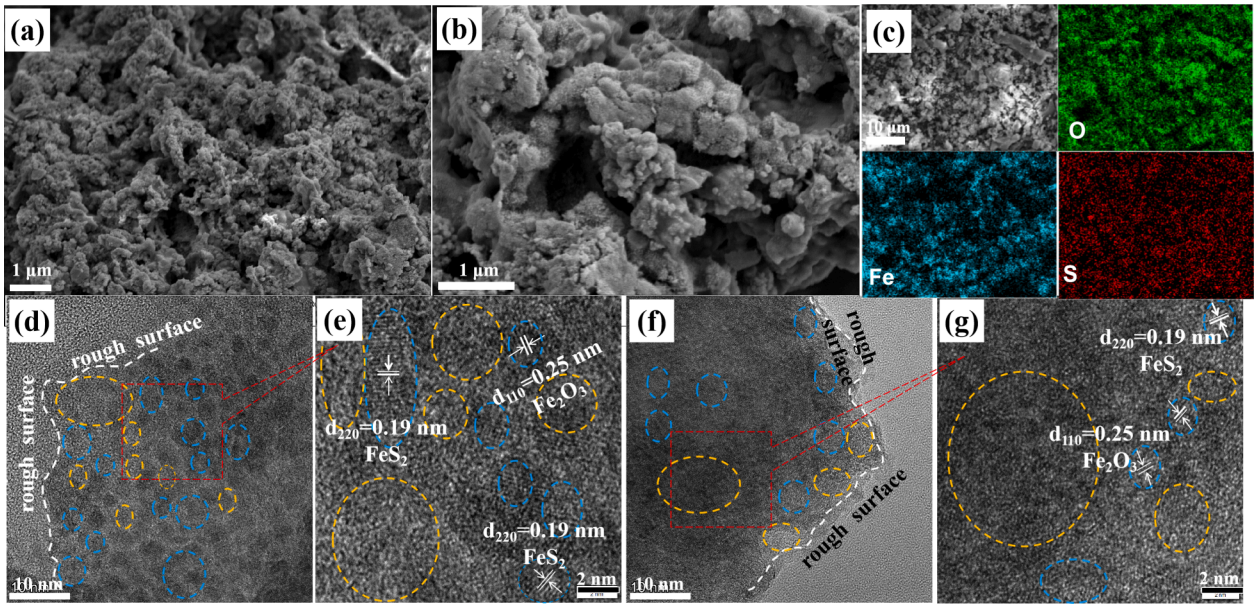

Fig. 6. (a-b) SEM, (c) elemental mapping (d, f) TEM, and (e, g) HRTEM of FeS_2 after OER.

Fig. 7d.

The EDX elemental analysis before and after OER was displayed in Fig. 7e. The relative content of S had reduced from 36.25 % to 1.77 % after OER. In contrast, the relative content of O increased from 3.28 % to 26.80 % after OER. In addition, the XRD patterns in Fig. 7f show that the obvious characteristic diffraction peaks for Fe_2O_3 and FeS_2 appeared, indicating that the FeS_2 have largely evolved into crystalline Fe_2O_3, further suggesting the reconstruction of the catalyst. The peak at 44.67° can be attributed to the Ni, because the catalysts were dropped onto the foam Ni. All the above discussion indicates that the FeS_2 catalysts with smooth surface and uniform dispersion have largely reconstructed to crystalline-amorphous Fe_2O_3/Fe-OOH.

Based on the above discussion, the synergistic effect of Co contents and reconstructing influence on Fe/S catalysts is put forward and is described in Scheme 2. First, the strong combination of Fe-S bond and the uniform dispersion of FeS_2 endow it improved charge transfer capability. During OER process, the FeS_2 with smooth surface has largely reconstructed to crystalline-amorphous Fe_2O_3/Fe-OOH with rough surface, which has a energy barrier for elementary reaction of O*→OOH*, further boosting the generation of O_2 (Su et al., 2024). As a result, the FeS_2 with fast electron transfer and low energy barrier for O*→OOH* exhibits excellent electrocatalytic water splitting capability towards OER.

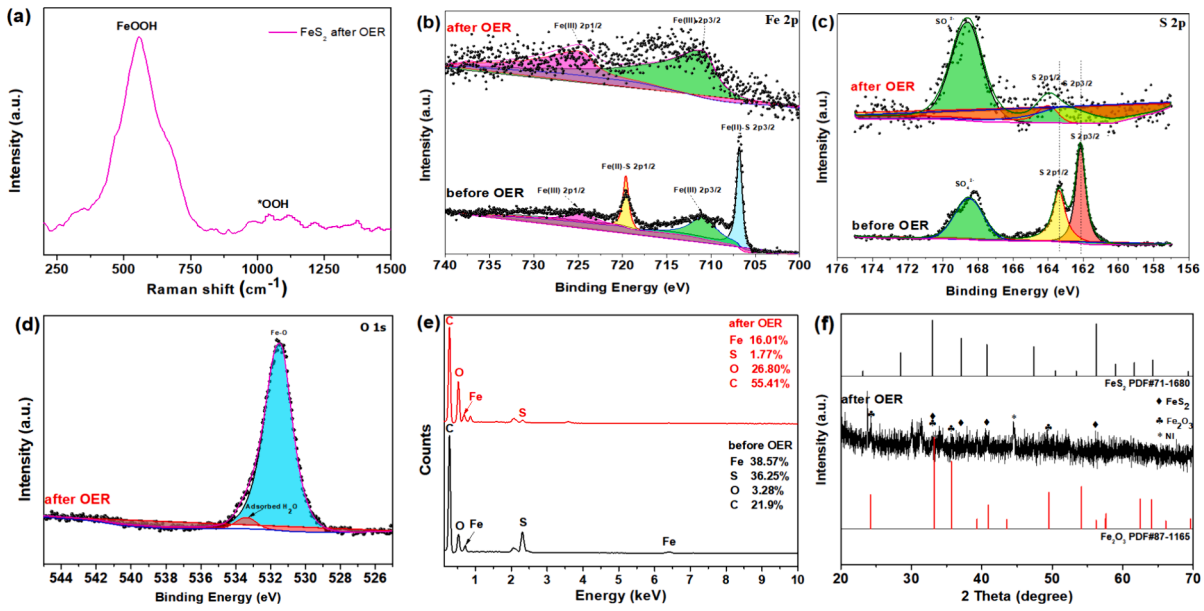

Fig. 7. (a) Raman spectrum of FeS_2 after OER process, XPS spectra of (b) Fe 2p (c) S 2p (d) O 1 s (e) the percentages of Fe, S, O, and C, (f) XRD patterns with FeS_2 after OER.

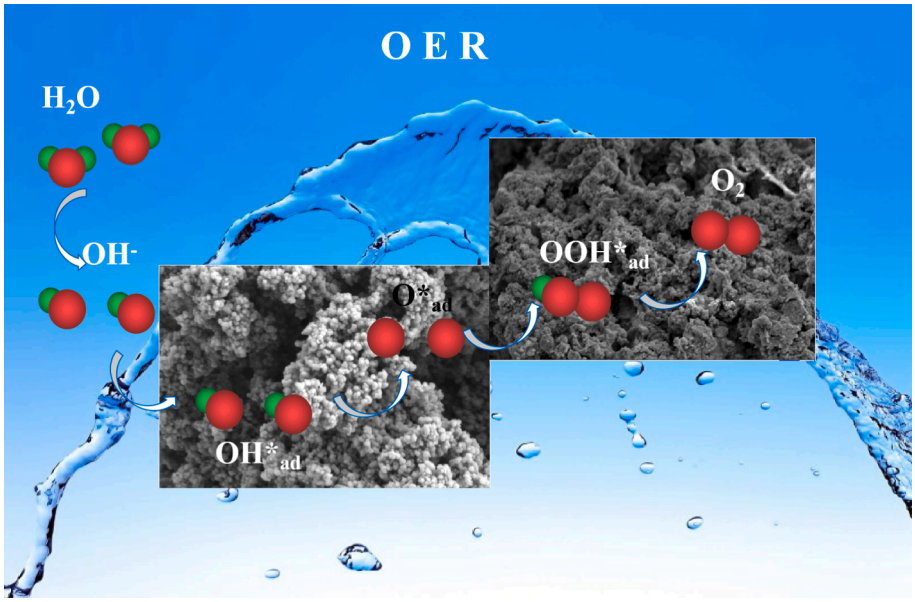

Scheme 2. OER process in FeS_2 electrocatalysts.

4. Conclusion

In this study, highly-efficient $Fe_xCo_{1-x}S_2$ (x = 0, 0.25, 0.5, 0.75 and 1) nanoparticles toward OER in alkaline electrolyte were designed. Remarkably, the FeS_2 delivered the most outstanding OER activity among prepared catalysts, with the overpotential of 240 mV for 10 mA/cm^2, ultra-low Tafel slope of 45 mV/decades and high stability for 16 h. XRD, SEM, HRTEM, Raman and XPS characteristics before and OER process, TOF and electrochemical results indicate that surface reconstruction, strong combination of F-S bonds and uniform dispersion of particles endow FeS_2 with excellent catalytic property. The FeS_2 with fast electron transfer and low energy barrier for O*→OOH* exhibits excellent electrocatalytic water splitting capability towards OER This study may provide a new idea for the research of metal sulfide electrocatalysts toward OER for alkaline water splitting systems.

CRediT authorship contribution statement

Xiaozhen Ren: Writing – review & editing, Writing – original draft, Investigation, Funding acquisition. **Shanshan Li:** Investigation, Formal analysis. **Ziyou Li:** Methodology, Investigation. **Zhenyang Zhang:** Methodology. **Hanxu Hou:** Methodology, Investigation. **Yanan Zhou:** Methodology, Investigation. **Chuanyu Jin:** Methodology, Investigation.

Declaration of Competing Interest

The authors declare that they have no known competing financial interests or personal relationships that could have appeared to influence the work reported in this paper.

Acknowledgements

This work was supported by the National Natural Science Foundation of China (Grant No. 51904148) and the Undergraduate Innovation Training Program Fund of Liaocheng University (Grant No. cxcy2022247).

Appendix A. Supplementary data

Supplementary data to this article can be found online at https://doi.org/10.1016/j.arabjc.2024.105907.

References

Abu-Zied, B.M., Ali, T.T., 2018. Fabrication, characterization and catalytic activity measurements of nano-crystalline Ag-Cr-O catalysts. Appl. Surf. Sci. 457, 1126–1135. https://doi.org/10.1016/j.apsusc.2018.06.237.

Chen, G., Hu, Z., Zhu, Y., Gu, B., Zhong, Y., Lin, H., Chen, C., Zhou, W., Shao, Z., 2018. A universal strategy to design superior water-splitting electrocatalysts based on fast in situ reconstruction of amorphous nanofilm precursors. Adv. Mater. 30, 1804333. https://doi.org/10.1002/adma.201804333.

Chen, L., Wang, Y.P., Zhao, X., Wang, Y., Li, Q., Wang, Q., Tang, Y., Lei, Y., 2022. Trimetallic oxyhydroxides as active sites for large-currentdensity alkaline oxygen evolution and overall water splitting. J. Mater. Sci. Technol. 110, 128–135. https://doi.org/10.1016/j.jmst.2021.08.083.

Fang, Z., Peng, L., Lv, H., Zhu, Y., Yan, C., Wang, S., Kalyani, P., Wu, X., Yu, G., 2017. Metallic transition metal selenide holey nanosheets for efficient oxygen evolution electrocatalysis. ACS Nano 11 (9), 9550–9557. https://doi.org/10.1021/acsnano.7b05481.

Feng, X., Jiao, Q., Liu, T., Li, Q., Yin, M., Zhao, Y., Li, H., Feng, C., Zhou, W., 2017. Facile synthesis of Co_9S_8 hollow spheres as a high-performance electrocatalyst for the oxygen evolution reaction. ACS Sustain Chem. Eng. 6, 1863–1871. https://doi.org/10.1021/acssuschemeng.7b03236.

Gong, M., Li, Y.G., Wang, H.L., Liang, Y.Y., Wu, J.Z., Zhou, J.G., Wang, J., Regier, T., Wei, F., Dai, H.J., 2013. An Advanced Ni−Fe Layered Double Hydroxide Electrocatalyst for Water Oxidation. J. Am. Chem. Soc. 135 (23), 8452–8455. https://doi.org/10.1021/ja4027715.

Guo, C.Y., Liu, X.J., Gao, L.F., Kuang, X., Ren, X., Ma, X.J., Zhao, M.Z., Yang, H., Sun, X., Wei, Q., 2020. Fe–doped Ni_2P nanosheets with porous structure for electroreduction of nitrogen to ammonia under ambient conditions. Appl. Catal. b: Environ. 263, 118296 https://doi.org/10.1016/j.apcatb.2019.118296.

He, S., Chen, B., Meng, C., Shi, F., Yuan, A., Miao, W., Zhou, H., 2024. Coupling $NiSe_2$ Nanoparticles with N-Doped Porous Carbon Enables Efficient and Durable Electrocatalytic Hydrogen Evolution Reaction at pH Values Ranging from 0 to 14. ACS Appl. Nano Mater. 7 (1), 1138–1145. https://doi.org/10.1021/acsanm.3c05126.

Huang, R., Chen, W., Zhang, Y., Huang, Z., Dai, H., Zhou, Y., Wu, Y., Lv, X., 2019. Welldesigned cobalt-nickel sulfide microspheres with unique peapod-like structure for overall water splitting. J. Colloid Interface Sci. 556, 401–410. https://doi.org/10.1016/j.jcis.2019.08.093.

Jiao, Y., Zheng, Y., Jaroniec, M., Qiao, S.Z., 2015. Design of electrocatalysts for oxygen- and hydrogen-involving energy conversion reactions. Chem. Soc. Rev. 44, 2060–2086. https://doi.org/10.1039/C4CS00470A.

Kang, H., Song, M., Yang, M., Lee, J., 2021. Lithium metal anode with lithium borate layer for enhanced cycling stability of lithium metal batteries. J. Power Sources 485, 229286. https://doi.org/10.1016/j.jpowsour.2020.229286.

Khani, H., Wipf, D.O., 2017. Iron oxide nanosheets and pulse-electrodeposited Ni-Co-S nanoflake arrays for high-performance charge storage. ACS Appl. Mater. Interfaces 9 (8), 6967–6978. https://doi.org/10.1021/acsami.6b11498.

Koza, J.A., Hull, C.M., Liu, Y.-C., Switzer, J.A., 2013. Deposition of β-$Co(OH)_2$ Films by Electrochemical Reduction of Tris(ethylenediamine)cobalt(III) in Alkaline Solution. Chem. Mater. 25 (9), 1922–1926. https://doi.org/10.1021/cm400579k.

Li, D., Li, Z.Y., Zou, R., Shi, G., Huang, Y.M., Yang, W., Yang, W., Liu, C.F., Peng, X.W., 2022. Coupling overall water splitting and biomass oxidation via Fe-doped Ni_2P@C nanosheets at large current density. Appl. Catal. b: Environ. 307, 121170 https://doi.org/10.1016/j.apcatb.2022.121170.

Li, Z., Xiao, M., Zhou, Y., Zhang, D., Wang, H., Liu, X., Wang, D., Wang, W., 2018. Pyrite FeS_2/C nanoparticles as an efficient bi-functional catalyst for overall water splitting. Dalton Trans. 47, 14917–14923. https://doi.org/10.1039/C8DT02927J.

Lin, Y., Chen, G., Wan, H., Chen, F., Liu, X., Ma, R., 2019. 2D free-standing nitrogen-doped Ni-Ni_3S_2 @carbon nanoplates derived from metal-organic frameworks for enhanced oxygen evolution reaction. Small 15, 1900348. https://doi.org/10.1002/smll.201900348.

Ma, X., Zhang, W., Deng, Y., Zhong, C., Hu, W., Han, X., 2018. Phase and composition controlled synthesis of cobalt sulfide hollow nanospheres for electrocatalytic water splitting. Nanoscale 10, 4816–4824. https://doi.org/10.1039/c7nr09424h.

Moysiadou, A., Lee, S., Hsu, C., Chen, H.M., Hu, X., 2020. Mechanism of oxygen evolution catalyzed by cobalt oxyhydroxide: cobalt superoxide species as a key intermediate and dioxygen release as a rate-determining step. J. Am. Chem. Soc. 142, 11901–11914. https://doi.org/10.1021/jacs.0c04867.

Nguyen, T.X., Su, Y.H., Lin, C.C., Ting, J.M., 2021. Self-reconstruction of sulfate-containing high entropy sulfide for exceptionally high-performance oxygen evolution reaction clectrocatalyst. Adv. Funct. Mater. 31, 2106229. https://doi.org/10.1002/adfm.202106229.

Peng, D.Q., Hu, C., Luo, X.F., Luo, J.L., Ding, Y., Ding, W.D., Ding, H., Ding, Y., Yu, T., Lei, W., Yuan, C.L., 2023. Electrochemical reconstruction of NiFe/NiFeOOH superparamagnetic core/catalytic shell heterostructure for magnetic heating enhancement of oxygen evolution reaction. Small 19 (3), 2205665. https://doi.org/10.1002/smll.202370014.

Pomerantseva, E., Bonaccorso, F., Feng, X., Cui, Y., Gogotsi, Y., 2019. Energy storage: The future enabled by nanomaterials. Science 366, eaan8285. https://doi.org/10.1126/science.aan8285.

Rebrov, E.V., Gao, P.-Z., 2023. Molecular Catalysts for OER/ORR in Zn–Air Batteries. Catalysts. 13, 1289. https://doi.org/10.3390/catal13091289.

Ren, X.Z., Li, S.S., Liu, J.C., Zhou, Y.N., Yin, J., Yang, H., 2023. Synergistic effect of surface reconstruction and rGO for FeS_2/rGO electrocatalysis with efficient oxygen evolution reaction for water splitting. Arab. J. Chem. 16, 105069 https://doi.org/10.1016/j.arabjc.2023.105069.

Su, Q.H., Sheng, R., Liu, Q.C., Ding, J., Wang, P.Y., Wang, X.C., Wang, J.L., Wang, Y.G., Wang, B., Huang, Y.D., 2024. Surface reconstruction of RuO_2/Co_3O_4 amorphous-crystalline heterointerface for efficient overall water splitting. J. Colloid Interf. Sci. 658, 43–51. https://doi.org/10.1016/j.jcis.2023.12.045.

Suen, N.T., Hung, S.F., Quan, Q., Zhang, N., Xu, Y.J., Chen, H.M., 2017. Electrocatalysis for the oxygen evolution reaction: recent development and future perspectives. Chem. Soc. Rev. 46, 337–365. https://doi.org/10.1039/C6CS00328A.

Wang, J., Bai, F., Chen, X., Lu, Y., Yang, W., 2017. Intercalated $Co(OH)_2$-derived flower-like hybrids composed of cobalt sulfide nanoparticles partially embedded in nitrogen doped carbon nanosheets with superior lithium storage. J. Mater. Chem. A 5, 3628–3637. https://doi.org/10.1039/C6TA10151H.

Wang, G., Cao, W., Zhang, Z., Liu, L., Wang, C., Yin, J., Zhou, H., 2023a. Ternary sulfide nanoparticles anchored in carbon bubble structure for oxygen evolution reaction. Journal of Alloys and Compounds 968, 172314. https://doi.org/10.1016/j.jallcom.2023.172314.

Wang, B., Hu, Y., Yu, B., Zhang, X., Yang, D., Chen, Y., 2019. Heterogeneous CoFe-Co_8FeS_8 nanoparticles embedded in CNT networks as highly efficient and stable electrocatalysts for oxygen evolution reaction. J. Power Sources 433, 126688. https://doi.org/10.1016/j.jpowsour.2019.05.094.

Wang, B., Chen, Y., Wang, X., Zhang, X., Hu, Y., Yu, B., Yang, D., Zhang, W., 2020a. A microwave-assisted bubble bursting strategy to grow Co_8FeS_8/CoS heterostructure on rearranged carbon nanotubes as efficient electrocatalyst for oxygen evolution reaction. J. Power Sources 449, 227561. https://doi.org/10.1016/j.jpowsour.2019.227561.

Wang, S.L., He, X.J., Wang, S.D., Huang, X., Wu, M.Y., Xiang, D.H., 2023c. $FeCoS_2$/Co_4S_3/N-doped graphene composite as efficient electrocatalysts for overall water splitting. Electrochim. Acta 441, 141790. https://doi.org/10.1016/j.electacta.2022.141790.

Wang, G., Jin, C., Zhang, G., Qian, L., Chen, X., Tan, J., Wang, W., Yin, J., Liu, X., Zhou, H., 2021. Surface self-reconstructed amorphous/crystalline hybrid iron disulfifide for high-effifffifficiency water oxidation electrocatalysis. Dalton Trans. 50, 6333–6342. https://doi.org/10.1039/d1dt00730k.

Wang, C., Shao, X., Pan, J., Hu, J., Xu, X., 2020b. Redox bifunctional activities with optical gain of Ni_3S_2 nanosheets edged with MoS_2 for overall water splitting. Appl. Catal. B Environ. 268, 118435 https://doi.org/10.1016/j.apcatb.2019.118435.

Wang, Y., Shen, G., Zhang, Y., Pan, L., Zhang, X., Zou, J.J., 2020d. Visible-light-induced unbalanced charge on NiCoP/TiO_2 sensitized system for rapid H_2 generation from hydrolysis of ammonia borane. Appl. Catal. b: Environ. 260, 118183 https://doi.org/10.1016/j.apcatb.2019.118183.

Wang, T., Wang, P., Zang, W., Li, X., Chen, D., Kou, Z., Mu, S., Wang, J., 2022. Nanoframes of Co_3O_4-Mo_2N Heterointerfaces Enable High-Performance Bifunctionality toward Both Electrocatalytic HER and OER. Adv. Funct. Mater. 32, 2107382. https://doi.org/10.1002/adfm.202107382.

Wang, G., Wang, C., Zhao, L., Qiao, F., Zhang, X., Wang, H., Wang, W., Yin, J., Zhou, H., Liu, X., 2023b. Completely reconfigured Fe1-xS/C ultra-thin nanocomposite lamellar structure for highly efficient oxygen evolution. Fuel. 341, 127686 https://doi.org/10.1016/j.fuel.2023.127686.

Wang, W., Xu, Y., Yao, J., Liu, X., Yin, Z., Li, Z., 2020c. Enhanced oxygen and hydrogen evolution performance by carbon-coated CoS_2-FeS_2 nanosheets. Dalton Trans. 49, 13352–13358. https://doi.org/10.1039/D0DT02671A.

Wang, Z., You, J., Zhao, Y., Yao, R., Liu, G., Lu, J., Zhao, S., 2023d. Research progress on high entropy alloys and high entropy derivatives as OER catalysts. J Environ. Chem. Eng. 11 (1), 109080 https://doi.org/10.1016/j.jece.2022.109080.

Wang, L., Zhou, Q., Pu, Z., Zhang, Q., Mu, X., Jing, H., Liu, S., Chen, C., Mu, S., 2018. Surface reconstruction engineering of cobalt phosphides by Ru inducement to form hollow Ru-RuPx-CoxP pre-electrocatalysts with accelerated oxygen evolution reaction. Nano Energy 53, 270–276. https://doi.org/10.1016/j.nanoen.2018.08.061.

Xie, Y., Yu, H., Deng, L., Amin, R.S., Yu, D., A.E., Maximov M.Y., Li L., ElKhatib K.M., Peng S.,, 2022. Anchoring stable FeS_2 nanoparticles on MXene nanosheets via interface engineering for efficient water splitting. Inorg. Chem. Front. 9, 662–669. https://doi.org/10.1039/D1QI01465J.

Xu, Y., Feng, T.T., Cui, Z.J., Guo, P.F., Wang, W.P., Li, Z.C., 2021. Fe_7S_8/FeS_2/C as an effifficient catalyst for electrocatalytic water splitting. Int. J. Hydrogen Energy 46, 39216–39225. https://doi.org/10.1016/j.ijhydene.2021.09.159.

Xu, H., Shang, H., Wang, C., Jin, L., Chen, C., Wang, C., Du, Y., 2020. Three-dimensional open CoMoOx/CoMoSx/CoSx nanobox electrocatalysts for efficient oxygen evolution reaction. Appl. Catal. B Environ. 265, 118605 https://doi.org/10.1016/j.apcatb.2020.118605.

Yan, Y., Li, A., Lu, C.X., Zhai, T.F., Lu, S.F., Li, W.M., Zhou, W., 2020. Double-layered yolk-shell microspheres with $NiCo_2S_4$-Ni_9S_8-C heterointerfaces as advanced battery-type electrode for hybrid supercapacitors. Chem. Eng. J. 396, 125316 https://doi.org/10.1016/j.cej.2020.125316.

Ying, J., Li, J., Jiang, G., Cano, Z.P., Ma, Z., Zhong, C., Su, D., Chen, Z., 2018. Metal-organic frameworks derived platinum-cobalt bimetallic nanoparticles in nitrogen-doped hollow porous carbon capsules as a highly active and durable catalyst for oxygen reduction reaction. Appl. Catal. b: Environ. 225, 496–503. https://doi.org/10.1016/j.apcatb.2017.11.077.

Yu, J., Cheng, G., Luo, W., 2017. Ternary nickel-iron sulfide microflowers as a robust electrocatalyst for bifunctional water splitting. J. Mater. Chem. A 5, 15838–15844. https://doi.org/10.1039/c7ta04438k.

Yue, C.Z., Zhang, X.N., Yin, J., Zhou, H.W., Liu, K., Liu, X., 2023. Highly efficient FeS_2@FeOOH core-shell water oxidation electrocatalyst formed by surface reconstruction of FeS_2 microspheres supported on Ni foam. Appl. Catal. b: Environ. 339, 123171 https://doi.org/10.1016/j.apcatb.2023.123171.

Zhang, Y., Cui, B., Qin, Z.T., Lin, H., Li, J.B., 2013. Hierarchical wreath-like Au–$Co(OH)_2$ microclusters for water oxidation at neutral pH. Nanoscale 5, 6826–6833. https://doi.org/10.1039/C3NR01735D.

Zhang L, Cao X, Guo C, 2023. A. Hassan, Y. Zhang, J. Wang. Interface and morphology engineering of Ru-FeCoP hollow nanocages as alkaline electrocatalyst for overall water splitting. J Environ. Chem. Eng. 11, 111373. DOi: 10.1016/j.jece.2023.111373.

Zhang, S.L., Guan, B.Y., Lu, X.F., Xi, S.B., Du, Y.H., Lou, X.W., 2020. Metal Atom-Doped Co_3O_4 Hierarchical Nanoplates for Electrocatalytic Oxygen Evolution. Adv. Mater. 32 (31), 2002235. https://doi.org/10.1002/adma.202002235.

Zhang, H., Zhou, Y., Xu, M., Chen, A., Ni, Z., Akdim, O., Wågberg, T., Huang, X., Hu, G., 2023a. Interface engineering on amorphous/crystalline hydroxides/sulfides heterostructure nanoarrays for enhanced solar water splitting. ACS Nano 17 (1), 636–647. https://doi.org/10.1021/acsnano.2c09880.